Strain-Based Fatigue Experimental Study on Ti–6Al–4V Alloy Manufactured by Electron Beam Melting

Alberto David Pertuz-Comas, Octavio Andrés González-Estrada, Elkin Martínez-Díaz, Diego Fernando Villegas-Bermúdez, Jorge Guillermo Díaz-Rodríguez

Journal of
Manufacturing and Materials Processing

MDPI

Article

Strain-Based Fatigue Experimental Study on Ti–6Al–4V Alloy Manufactured by Electron Beam Melting

Alberto David Pertuz-Comas [1], Octavio Andrés González-Estrada [2,*], Elkin Martínez-Díaz [3], Diego Fernando Villegas-Bermúdez [2] and Jorge Guillermo Díaz-Rodríguez [2]

[1] GIC, School of Mechanical Engineering, Universidad Industrial de Santander, Carrera 27 Calle 9, Bucaramanga 680002, Colombia
[2] GIEMA, School of Mechanical Engineering, Universidad Industrial de Santander, Carrera 27 Calle 9, Bucaramanga 680002, Colombia
[3] AIDIMME, KAMAX S.L.U., 46136 Museros, Spain
* Correspondence: agonzale@uis.edu.co

Abstract: Additive manufacturing (AM) by electron beam melting (EBM) is a technique used to manufacture parts by melting powder metal layer-by-layer with an electron beam in a high vacuum, thereby generating a 3D topology. This paper studies the low-cycle fatigue of Ti–6Al–4V specimens obtained by EBM. Static tests were carried out according to ASTM E8 for a yield stress of 1023 MPa, a fracture stress of 1102 MPa, and a maximum tensile strength of 1130 MPa with a maximum true normal strain at fracture ε_{max} = 9.0% and an elastic modulus of 120 GPa. Then, fatigue tests were conducted at a load inversion rate of R = −1. It was observed that the material exhibited plastic strain softening, which was attributed to the Bauschinger effect. These results were plotted on a strain vs. life ($\varepsilon-N$) curve using the Ong version of the Coffin–Manson rule and the Baumel–Seager and Meggiolaro–Castro rules. The results were compared to forged Ti–6Al–4V alloys. The cyclic stress–strain behavior was described with the Ramberg–Osgood model. Finally, the fracture surface was analyzed using scanning electron microscopy (SEM) to observe the formation of primary cracks. The fracture morphology showed a mixed surface, also known as a "quasi-cleavage", which is characterized by dimples, cleavage facets, extensive primary cracks with broken slipping planes, and a large number of inclusions. This phenomenon caused a possible brittle behavior in the material.

Keywords: additive manufacture; low-cycle fatigue; Ti–6Al–4V; electron beam melting; crack initiation

Citation: Pertuz-Comas, A.D.; González-Estrada, O.A.; Martínez-Díaz, E.; Villegas-Bermúdez, D.F.; Díaz-Rodríguez, J.G. Strain-Based Fatigue Experimental Study on Ti–6Al–4V Alloy Manufactured by Electron Beam Melting. *J. Manuf. Mater. Process.* **2023**, *7*, 25. https://doi.org/10.3390/jmmp7010025

Academic Editors: Mohsen K. Keshavarz and Esmaeil Sadeghi

Received: 19 December 2022
Revised: 13 January 2023
Accepted: 16 January 2023
Published: 18 January 2023

1. Introduction

Additive manufacturing (AM) enabled the transition from subtractive to additive fabrication [1], which allowed for the fabrication of parts with very complex functional geometries and offered lower manufacturing costs [2]. One of the AM techniques for metals is electron beam melting (EBM). This technique uses an electron beam to selectively melt a bed of metallic powder directed by the computer-aided design (CAD) model [3,4]. Such directional melting may leave high rugosity and residual stresses [5] and have an effect on the microstructure and mechanical properties [6]. One commonly used metal in EBM AM is Ti and the Ti–6Al–4V alloy [7,8]. Its relatively low density and high rupture stress give it an excellent resistance to density ratio [9]. It was initially developed for the aerospace industry in the 1950s and is one of the metals with the best biocompatibility for biomechanical applications [8,10–12]. However, such applications involve fluctuating stresses. Therefore, EBM-manufactured materials should be characterized accordingly to withstand such loading conditions. This paper presents strain–life (ε–N_f) experiments for machined but not stress-relieved specimens. The data were adjusted to appropriate models along with a fractographic analysis.

1.1. Manufacturing Process

EBM is an AM process that melts metal powder beds. As with any AM technique, a topology is loaded into slicing software that decomposes the geometry into layers with a defined thickness [13]. A typical EBM equipment schematic is shown in Figure 1.

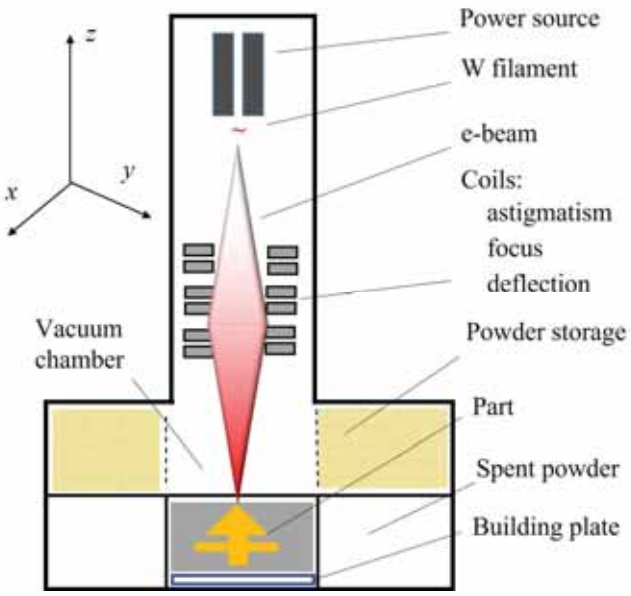

Figure 1. Schematics of EBM.

Some advantages of metal AM are high reproducibility, which has virtually no tooling costs, where the cost of one part or many is about the same [14], and the feasibility of manufacturing complex parts with little or no post-processing [2,13]. Furthermore, in EBM, the electron can penetrate the powdery material; this feature uniformly heats the metal powder core and not just the surface, which could not be the case with reflective materials, leaving them partially melted. According to León et al. [13], AM could close the gap between topological optimization and the final product by eliminating the constraint imposed by the geometric complexity and the need for post-processing that is required by traditional manufacturing processes. On the other hand, some disadvantages of metal AM include the following: intrinsic porosity, surface roughness [15–17], oxygen contamination, and tensile residual stresses [4,10] produced by cooling rates as high as 10^4 °K/s [10]. Besides those, porosity might be the primary source of crack nucleation [17], which is the fatigue stage that usually takes the longest time [2]. Moreover, high residual stress is characteristic of metal AM due to the substantial thermal gradients [4,10]. Furthermore, ref. [10] showed that periodic beams passing through solidified powers produce liquid–solid and α–β transformations [1], which might induce microdentritic formation and, as a result, residual stresses.

1.2. Low-Cycle Fatigue

Low-cycle fatigue is understood as a material's behavior under cyclic elastic and plastic strain, which produces crack initiation. The Coffin–Mason rule, shown in Equation (1), is commonly accepted [9] to describe the strain–cycle (ε–N_f) relationship or low-cycle fatigue (LCF). A structural component subjected to repetitive loads above yield strain experiences elastic and plastic deformations.

$$\frac{\Delta\varepsilon}{2} = \frac{\Delta\varepsilon_e}{2} + \frac{\Delta\varepsilon_p}{2} = \sigma'_f\left(2N_f\right)^b + \varepsilon'_f\left(2N_f\right)^c \quad (1)$$

where ε is the strain, σ the stress, N_f is the number of cycles to failure, σ'_f is the true stress calculated with the instant area, and the subscripts p and e refer to plastic and elastic, respectively, and b and c are the material-dependent constants. Furthermore, Meggiolaro and Castro [18] evaluated the Coffin–Mason type of rules for more than 845 alloys, establishing "rules of thumb" for several groups. They found the Baumel–Seager model best describes the low-cycle fatigue regime for Ti and Al alloys, which is shown in Equation (2) as follows:

$$\frac{\Delta\varepsilon}{2} = \frac{\Delta\varepsilon_e}{2} + \frac{\Delta\varepsilon_p}{2} = 0.35\left(2N_f\right)^{-0.69} + \frac{1.67\sigma_u}{E}\left(2N_f\right)^{-0.095} \quad (2)$$

Furthermore, the same authors [18] proposed a rule for Ti alloys but with optimized constants, which is shown in Equation (3) as follows:

$$\frac{\Delta\varepsilon}{2} = \frac{\Delta\varepsilon_e}{2} + \frac{\Delta\varepsilon_p}{2} = 0.28\left(2N_f\right)^{-0.66} + \frac{1.9\sigma_u}{E}\left(2N_f\right)^{-0.11} \quad (3)$$

Research has been performed to understand the Ti–6Al–4V fatigue behavior produced by AM. Chastand et al. [19] tested the alloy, which was printed by selective laser melting (SLM) and EBM, and found that anisotropy is negligible after 6000 cycles, except when the loading is parallel to the beam. Agius et al. [20] compared SLM and wrought alloys and reported that the second showed significantly higher plastic work than the SLM. Bourell et al. [21] reviewed results from several AM techniques and concluded that as-processed surfaces had a reduced life because stress concentrations accelerate crack nucleation and growth. Kasperovich and Hausmann [22] tested SLM specimens at 82 Hz under full stress inversion, producing fatigue lives as high as 1×10^7 cycles. Le et al. [23] also tested specimens printed on SLM but at 90° of the loading orientation at HCF. Furthermore, refs. [19,21,24] discussed failure mechanisms in metal AM, and [3,10] provided an extensive description of microstructures. Moreover, porosity in metal AM is attributed to either trapped inert gas pores, a lack of fusion [3,10] in areas between adjacent beam passes, which can accelerate the crack nucleation phase [22], or insufficient local melting power [25]. Additionally, refs. [17,26–29] published fatigue data for Ti–6Al–4V alloys printed by EBM, but only under high-cycling regimes. Refs. [3,10] reviewed the mechanical properties and testing for Ti–6Al–4V alloys printed by several AM techniques, and [30] focused their analyses on uniaxial tests that produced HCF affected by build orientation and heat treatment surface finishing. Sterling et al. [31] reported low-cycle fatigue tests, but for LENS. Bressan et al. [32] reported tests under proportional and non-proportional loads for selective laser sintering (SLS). Benz et al. [33] performed fatigue tests on EBM-printed specimens. To date, refs. [33–36] have performed uniaxial strain–life on Ti–6Al–4V alloys manufactured by EBM. Table 1 shows a summary of reported tests for different AM Ti–6Al–4V alloys. It can be seen that most of the testing is focused on tensile tests and fatigue in the high-cycle regime. This study proposes a strain–life approach, including testing as little as 115 cycles, to enhance the parameters associated with large deformations in components presenting highly localized stresses, where crack initiation may occur.

This paper illustrates uniaxial strain–life tests for EBM-manufactured Ti–6Al–4V alloys under LCF at R = −1. The characteristic AM rugosity was removed by machining, but the specimens were not stress-relieved, leaving what we believe is the differential characteristic given by AM. It describes the process of obtaining the parameters for modeling such behaviors and explains the fractured specimen's morphology. Finally, the results are compared with forged stock materials, revealing some notable differences.

Table 1. Summary of relevant tests for AM Ti–6Al–4V alloys. LCF, low-cycle fatigue; HCF, high cycle fatigue; VHCF, very high cycle fatigue; SEM, scanning electron microscopy; XRD, X-ray diffraction; LS, laser sintering; HV, Vickers hardness.

Author	Year	Method	Tests	Fatigue Modeling	Comments
Kasperovich and Hausmann [22]	2015	EBM	tension, HCF, SEM, HV	N/A	heat treatment, R = −1
Sterling et al. [31]	2015	LENS	Tension, LCF, SEM	Coffin-Manson & Ramberg-Osgood	R = −1
Galarraga et al. [37]	2016	EBM	Tension, SEM	N/A	Different cooling ratios
Carrion [36]	2016		Tension		Different loading ratios
Fatemi et al. [15]	2017	PBF	torsion, HCF	N/A	heat treatment, R = −1
Günther et al. [17]	2017	SLM	HCF, VHCF, SEM	N/A	heat treatment
		EBM	HCF, VHCF, SEM	N/A	as built
Agius et al. [20]	2017	SLM	tension, LCF, SEM, XRD	Frederick-Amstrong	as-built material, different R ratios
Hrabe et al. [26]	2017	EBM	Tension, microstructure, HCF, residual stresses	N/A	as-built, heat treatment, R = 0.1
Kahlin et al. [27]	2017	EBM	HV, HCF, roughness, SEM	N/A	notch sensitivity, R = 0.1
		LS	HV, HCF, roughness, SEM	N/A	notch sensitivity, R = 0.1
Chastand et al. [19]	2018	SLM	Tension, HCF, SEM	N/A	Different printing orientations, heat treatment, and surface finishing
		EBM	Tension, HCF, SEM	N/A	Different printing orientations, heat treatment, and surface finishing
Bressan et al. [32]	2019	SLS	Multiaxial fatigue	N/A	Proportional and non-proportional load
Le et al. [23]	2020	SLM	Tension, HCF, X-ray tomography, SEM	Wöhler	R = 0.1
Benz et al. [33]	2020	EBM	Tension, Fatigue, SEM	Coffin–Manson and Johnson–Cook	+1000 cycles
Toasa et al. [29]	2021		Stüssi	N/A	Different stress ratio
Zhang et al. [35]	2022	EBM, SLS			
Bai et al. [34]	2022	EBM		Coffin-Manson	

2. Materials and Methods

Commercial Ti–6Al–4V powders supplied by Arcam (Arcam AB, Mölndal, Sweden) with spherical morphology, obtained by gas atomization, and with a size distribution between 45 and 100 μm were used in this study. Figure 2a,b shows details of the powder morphology at 100× and 400× magnification, respectively.

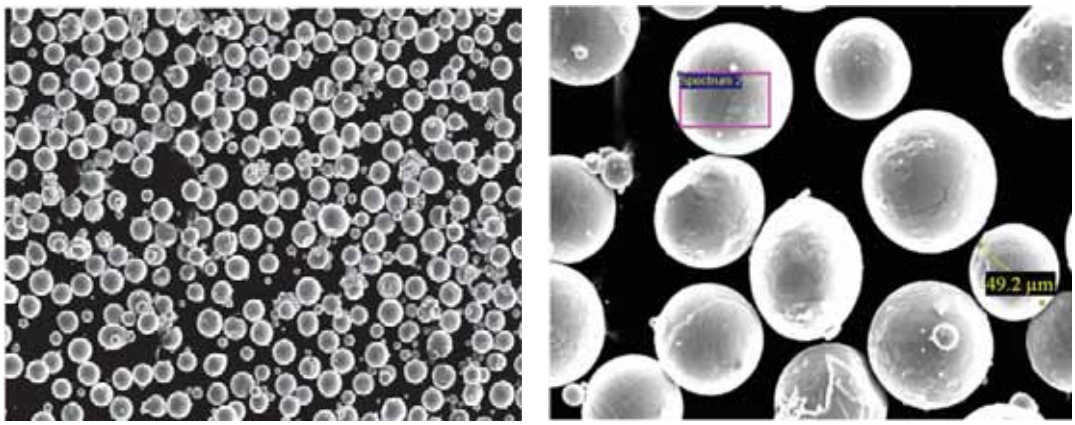

Figure 2. Ti–6Al–4V spherical powder morphology: (**a**) 100×; (**b**) 400×.

As indicated by Liu and Shin [10], a non-melted powder sphere is the shape that minimizes stress concentration factors as opposed to acicular particles, which are more frequently present in conventional casting processes. Table 2 presents the powder's chemical composition (% by weight) as given by the manufacturer and obtained with the ASTM F2924 standard.

Table 2. Chemical composition (% by weight) of the Ti–6Al–4V powder as given by the manufacturer.

Element	Al	V	C	Fe	O	N	H	Y	Ti
ASTM F2924	5.50–6.75	3.50–4.50	Max. 0.08	Max. 0.30	Max. 0.20	Max. 0.05	Max. 0.015	Max. 0.005	Bal.
% weight	6.48	3.96	0.01	0.15	0.14	0.01	0.004	<0.001	Bal.

The material was printed as cylindrical 64 mm and 120 mm long bars for fatigue and static tests, respectively, both with a diameter of 17.5 mm. Subsequently, the bars were CNC-machined according to the ASTM E8 standard. Figure 3a shows a view of the specimen as printed. Figure 3b shows the machined specimen dimensions for the fatigue specimens. A total of 5 specimens for static and 12 for fatigue were tested. Figure 3c shows an example of a test specimen mounted onto an MTS servo-hydraulic machine. Finally, Figure 3d shows the machined specimen dimensions for the static specimens.

First, tensile tests were conducted at a 1 mm/min crosshead rate until a fracture was observed. Afterward, the engineering and true stress, σ'_f, were both calculated. The true strain was calculated as a function of the instantaneous elongation using an axial extensometer. Secondly, fatigue tests were conducted at a full inversion ratio, R = −1, at 5 Hz under strain control. Finally, the strains were calculated over the original gauge length; the engineering and true stress were calculated with the initial and final cross-sectional areas, respectively. The fatigue tests were conducted at ±5.54, ±3.26, ±2.88, and ±2.26% of the engineering strain.

A universal MTS Bionix® servo-hydraulic Test Systems model 370.02 (MTS Systems, Eden Prairie, MN, USA) machine equipped with a 25 kN load cell was used with a 634.12F 25-mm axial extensometer. The tests were performed at room temperature, ranging from 23 to 26 °C approximately, with a 900 psi gripping pressure. The fatigue tests were recorded using MTS TestSuite™ ((Minneapolis, MN, USA). Finally, the fractured surfaces were examined with a Quanta FEG® 650 SEM (Thermo Fisher Scientific, Waltham, MA, USA).

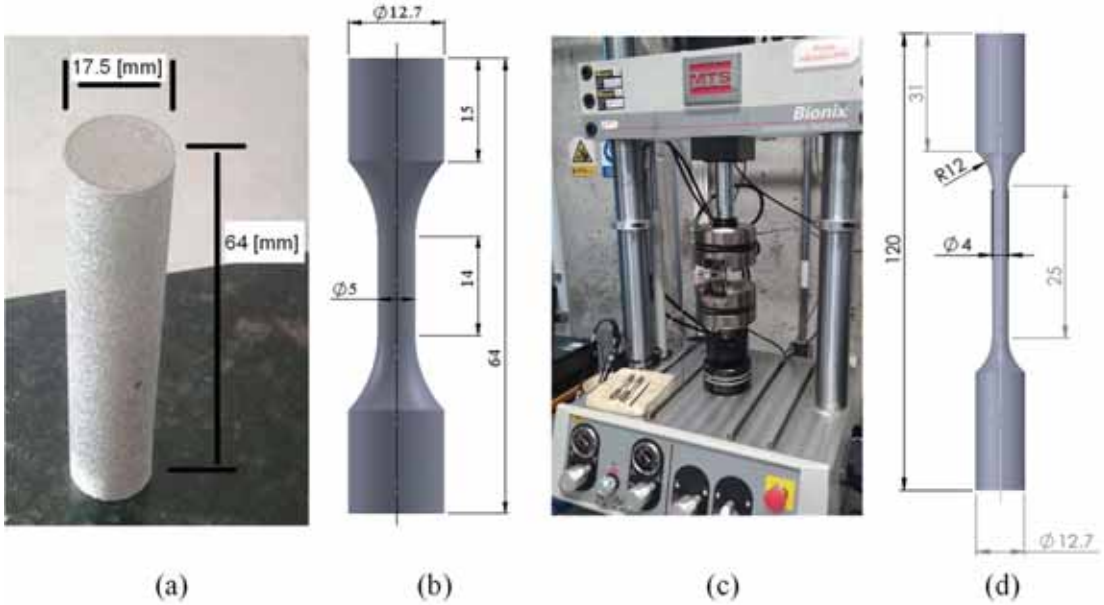

Figure 3. Test specimens: (**a**) as printed by EBM; (**b**) machined dimensions (mm) for fatigue tests; (**c**) testing of a specimen with an extensometer; (**d**) machined dimensions (mm) for static tensile tests.

3. Results

3.1. Microstructure

The Ti–6Al–4V specimens built by EBM were cut and placed in resin. They were gradually polished, up to 2000 sandpaper, and then polished with alumina powder from 0.3 to 0.1 μm. They were then acid attacked with Kroll's reagent (6% HNO_3, 2% HCF vol) for 20 s. The microstructure was observed with a reflection optical microscope, evaluating the following characteristics:

- Grain size: columnar grains in the *XZ* plane and faceted grains in the *XY* plane
- The thickness of the grain edge of the phase α between the grains β.
- The α plate thickness and α colony size (aspect ratio).

Figure 4a,b shows the Ti–6Al–4V alloy's as-built microstructure in the *XY* plane, whereas Figure 4c,d shows it for the *XZ* plane.

The microstructure was formed by β columnar (shown in black) grains oriented in the manufacturing direction (*XZ* plane), and this characteristic is a direct consequence of the high thermal gradient that exists in the *Z*-direction, as pointed out by [30]. The fabrication plate and deposited material act as a heat sink during the process, whereas the manufactured part is surrounded by loose/lightly sintered Ti powder that acts as an insulator. As such, heat losses are dominated in one dimension, along the *Z*-axis. A lamellar microstructure α + β was observed within the grains β for the planes both perpendicular and parallel to the manufacturing direction, which was also reported by Chern et al. [30]. Such a fine microstructure was responsible for the high strength found; see Figure 5. The lamellar structure was mainly Widmanstätten, with a random microstructure of colonies, also reported in [26]. The thickness of the plates/slats α was about 1.4 μm, which is very similar to that found by Galarraga et al. [37]. The presence of α grain edges along the grain boundaries of the previous phase suggested the diffusive nature of the transformation $\beta \rightarrow \alpha$ [25]. The microstructure observed in parts made with EBM differs from that obtained in other AM technologies, such as SLM, which shows extremely fast cooling rates [3], resulting in a martensitic transformation $\beta \rightarrow \alpha$ without diffusion. Overall, it seems that there is a structure produced by the 3D printing and another underlying one produced by the grain growth during the melting of the consecutive layers [5]. However, such analysis

is beyond the scope of the paper. Finally, some porosities (not shown) were observed in the micrographs and are extensively documented [1,4].

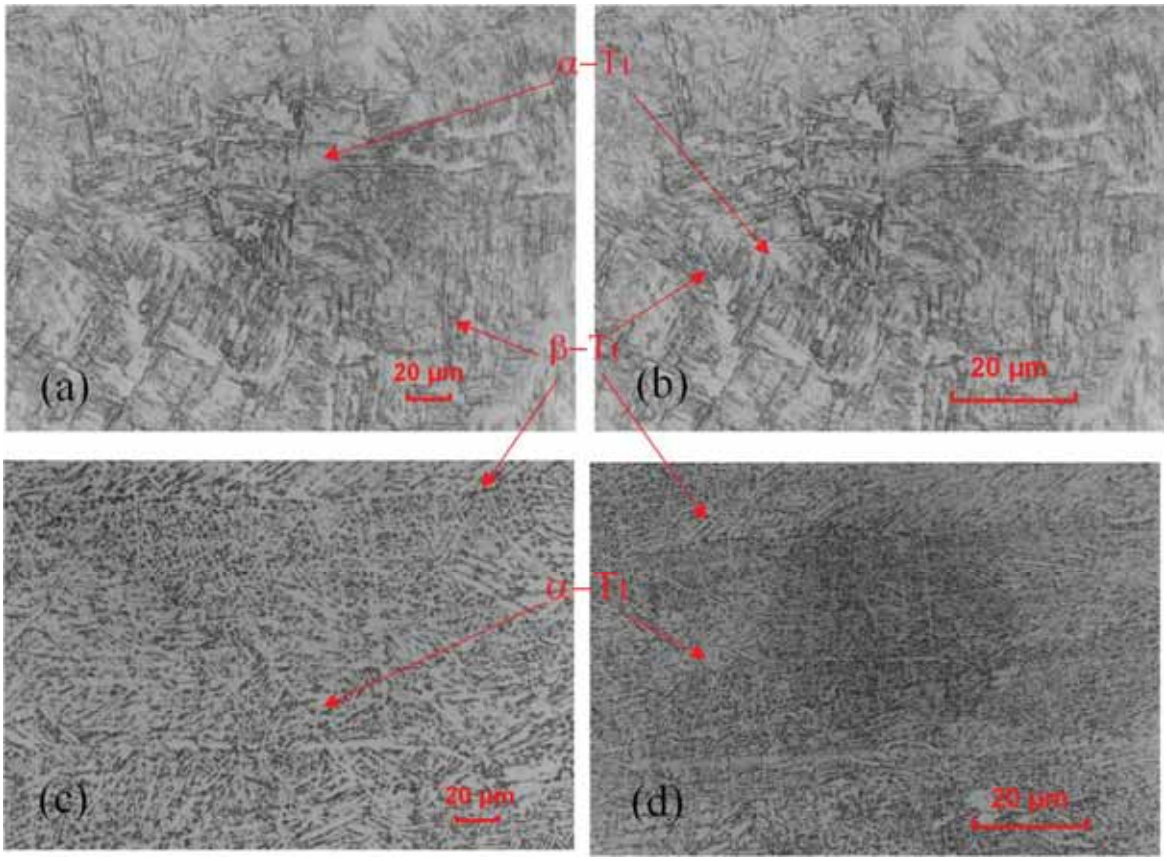

Figure 4. Microstructure of the Ti–6Al–4V alloy in the manufacturing state (as built). (**a**) *XY* plane 500×; (**b**) *XY* plane 1000×; (**c**) *XZ* plane 500×; (**d**) *XZ* plane 1000×.

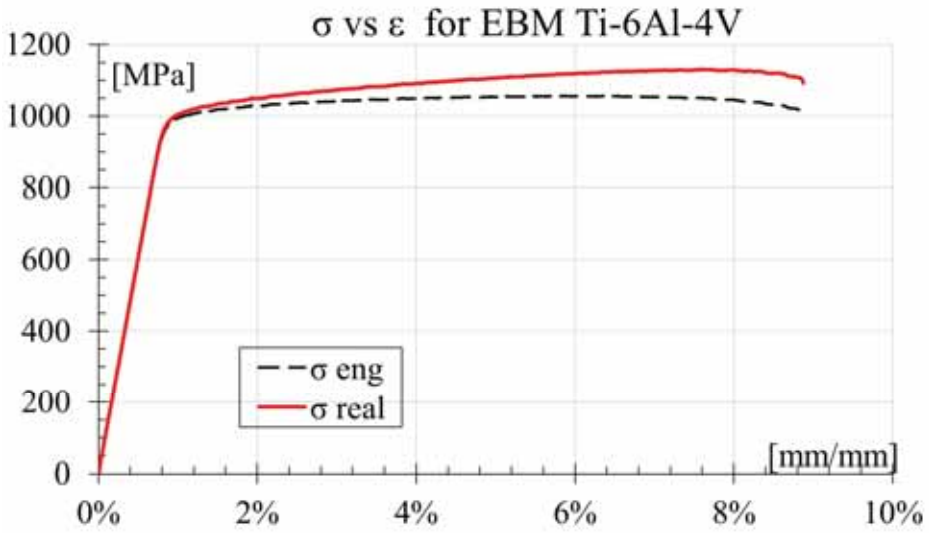

Figure 5. Engineering and real stress–strain curves for the EBM Ti–6Al–4V alloy.

3.2. Tensile Test

Table 3 shows the results from the tensile tests for the five specimens of the Ti–6Al–4V alloy obtained by EBM. The mean, median, min, max, and standard deviation (SD) values are reported for the yield stress σ_y, ultimate stress σ_u, breaking stress σ_f , and elastic modulus E. Figure 5 shows the exemplary engineering and real stress–strain results for the Ti–6Al–4V alloy obtained by EBM. The engineering stress curve exhibited a possible elastic–plastic behavior with a yield stress σ_y = 1023 MPa and an ultimate stress σ_u = 1130 MPa. Similar results are reported in [31], but slightly higher than those reported in [28,33,38]. Nevertheless, this material also had an elongation in the plastic regime of 8.2% for a total of 9.0%, which is slightly higher than that reported in [28,31]. Furthermore, the ratio for σ_u/σ_y is 1.1, which may indicate that the material softens under cyclic loading. Finally, the elastic modulus was 121 GPa.

Table 3. Mechanical properties for the tensile test specimens of the Ti–6Al–4V alloy obtained by EBM.

Specimen	σ_y (MPa)	σ_u (MPa)	σ_f (MPa)	E (GPa)
1	985	1088	971	124
2	1035	1142	1258	125
3	1031	1134	1061	120
4	1038	1151	1087	116
5	1025	1133	1135	118
Mean	1023	1130	1102	121
Median	1031	1134	1087	120
Min.	985	1088	971	116
Max.	1038	1151	1258	125
SD	22	25	105	4

3.3. Fatigue Tests

The fatigue tests were performed at a load inversion of R = −1 under constant displacement, which generated an accumulated cyclic plastic deformation, causing the material to soften to the point of rupture. Figure 6 shows the exemplary behavior of the hysteresis loops for 2, 25, 70, 80, and 85 cycles in a specimen subjected to ±5.54% of static strain, where the Bauschinger effect can be observed. The Bauschinger effect is observed when the yield strength of a polycrystalline metal decreases once the direction of the acting strain is inverted [9]. The area inside the stress−strain loop represents the specific net energy spent deforming the specimen. It can be seen that the material first experiences a slight plastic hardening of up to 25 cycles, as the area in that loop is smaller than the area contained in the two-cycle loop. Then, deformation causes the material to decay and experience plastic softening until rupture. The area inside the 70-cycle loop is more significant than the former; thus, the material has relaxed. It is an apparent brittleness due to the high residual stresses left by the EBM manufacturing process. When the Bauschinger effect occurs, the phenomenon experienced by the material is volumetric. Subsequently, after the volumetric deformation, a localized deformation begins, and it is at this moment that the fatigue phenomenon starts. Although the volumetric part takes a few cycles, that is why we can see the hysteresis loop.

Figure 7 depicts the hysteresis loop for a specimen subjected to ±3.26 of static strain for 2, 220, 350, 408, and 415 cycles. Although the subject deformation is lower than the one depicted in Figure 6, an almost identical behavior can be seen. As the load acts over time, the material softens.

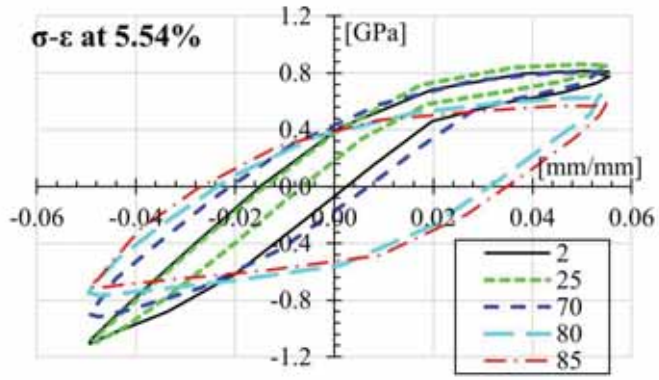

Figure 6. Exemplary result for the hysteresis loops at ±5.54% ε.

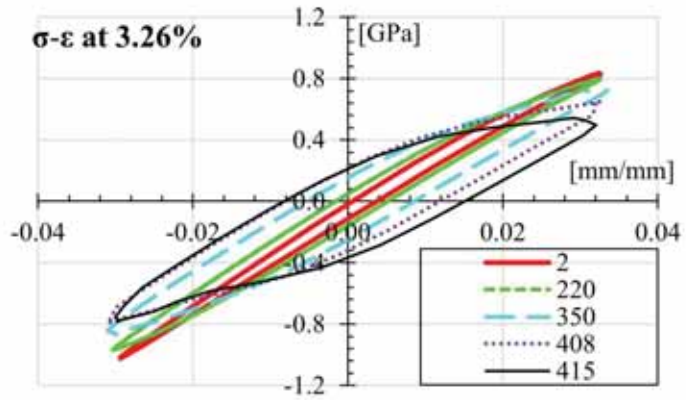

Figure 7. Exemplary result for the hysteresis loops at ±3.26% ε.

Figure 8 depicts the hysteresis loop for a specimen subjected to ±2.88 of static strain for 2, 10, 1200, and 2514 cycles. In this case, the subject deformation is significantly lower than the one depicted in Figure 7, as the loading and unloading paths follow almost the same track. However, a reduction in the stress and strain can be seen, which indicates the Bauschinger effect. Moreover, it is visible how the area inside the loops grows slightly as the material is subjected to more loading cycles.

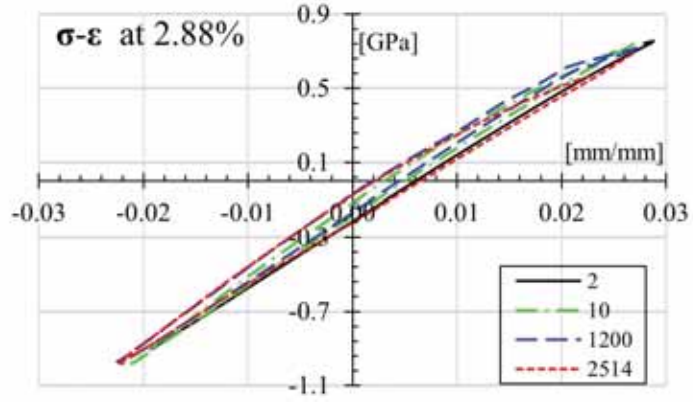

Figure 8. Exemplary result for the hysteresis loops at ±2.88% ε.

Figure 9 shows the hysteresis loop for a specimen subjected to ±2.26% of static strain for 2, 3000, and 6023 cycles. Although there is almost no plastic work, as the loading and

unloading tracks follow almost the same path, there is a slight difference in strain between the beginning and end cycles. The final strain is slightly smaller than the initial strain. Moreover, it is visible how the area inside the loops stays about the same size as the material is subjected to more loading cycles.

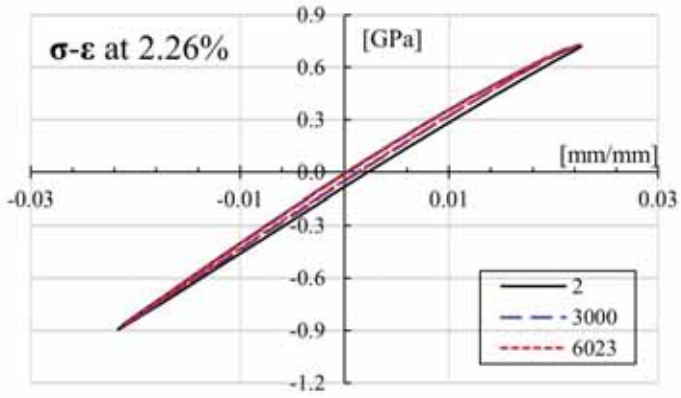

Figure 9. Exemplary result for the hysteresis loops at ± 2.26% ε.

From the hysteresis loops, the strain amplitude is obtained for the specimen until failure occurs, *Nf*, as presented in Table 4. Furthermore, the values for elastic and plastic strain ($\Delta\varepsilon_e$ and $\Delta\varepsilon_p$, respectively) for the Coffin−Mason (CM) Equation (1), Baumel−Seager (BS) Equation (2), and Meggiolaro−Castro (MC) Equation (3) are presented in Table 4.

Table 4. Measured cycles and strain for the fatigue tests and constants for the Coffin−Manson, Baumel−Seager, and Meggiolaro−Castro models.

% ε	N_f	Coffin−Manson			Baumel−Seager			Meggiolaro−Castro		
		$\Delta\varepsilon_p$	$\Delta\varepsilon_e$	$\Delta\varepsilon$	$\Delta\varepsilon_p$	$\Delta\varepsilon_e$	$\Delta\varepsilon$	$\Delta\varepsilon_p$	$\Delta\varepsilon_e$	$\Delta\varepsilon$
5.54	115	0.00085	0.00000	0.0017	0.00821	0.00949	0.01770	0.0266	0.0077	0.0172
	122	0.00083	0.00000	0.0017	0.00788	0.00944	0.01732	0.0265	0.0074	0.0170
	226	0.00059	0.00000	0.0012	0.00515	0.00890	0.01405	0.0247	0.0050	0.0148
3.26	414	0.00038	0.00000	0.0008	0.00339	0.00840	0.01180	0.0231	0.0033	0.0132
	417	0.00034	0.00000	0.0007	0.00338	0.00840	0.01177	0.0231	0.0033	0.0132
	736	0.00025	0.00000	0.0005	0.00228	0.00796	0.01024	0.0217	0.0023	0.0120
2.88	1512	0.00017	0.00000	0.0003	0.00139	0.00743	0.00882	0.0201	0.0014	0.0107
	2516	0.00013	0.00000	0.0003	0.00098	0.00708	0.00806	0.0190	0.0010	0.0100
	5511	0.00008	0.00000	0.0002	0.00057	0.00657	0.00714	0.0174	0.0006	0.0090
2.26	6023	0.00008	0.00000	0.0002	0.00053	0.00652	0.00705	0.0172	0.0006	0.0089
	7210	0.00008	0.00000	0.0002	0.00047	0.00640	0.00688	0.0169	0.0005	0.0087
	13335	0.00005	0.00000	0.0001	0.00031	0.00604	0.00635	0.0158	0.0003	0.0081

Figure 10 presents the tested alloy's strain $\Delta\varepsilon$ and failure cycle *Nf* results. For comparison, the low-cycle fatigue results for the as-forged Ti−6Al−4V alloy [9] and the modeling with MC are presented. It can be seen how the correlation model is conservative for short lives as it predicts smaller deformations [18] than the BS and MC. Moreover, comparing the fatigue curves obtained by EBM and as-forged [9], it can be seen that EBM's fatigue performance is slightly below that of the as-forged for short lives. However, after about 7000 cycles, the EBM and as-forged lives started to match.

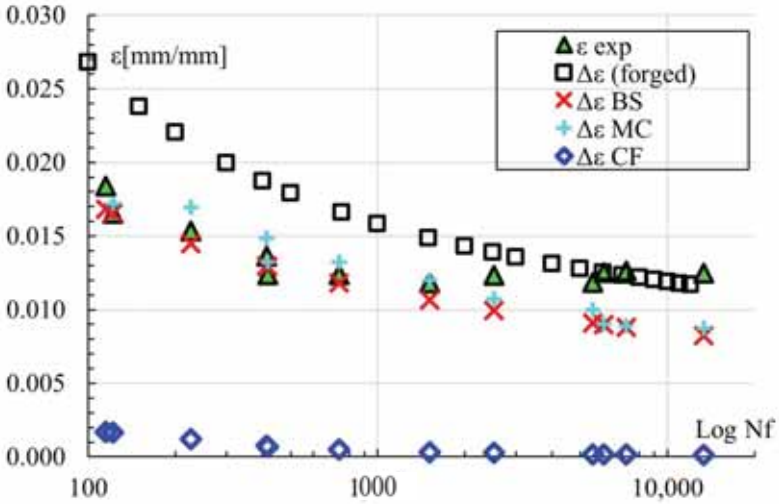

Figure 10. ε vs. N_f for the Ti−6Al−4V alloy obtained by EBM and as-forged.

3.4. Fractured Surface Morphology Analysis

Figure 11a shows the macroscopic photograph of a tensile test. It shows how the specimen presents a failure plane of approximately 45°. Figure 11b shows an outer ring that is typical for cleavage fractures with shear lips planes. Such a macroscopic type of failure has been reported in [22,31] for this alloy. However, large and visible deformations are usually visible before ductile fractures, which is not the case here.

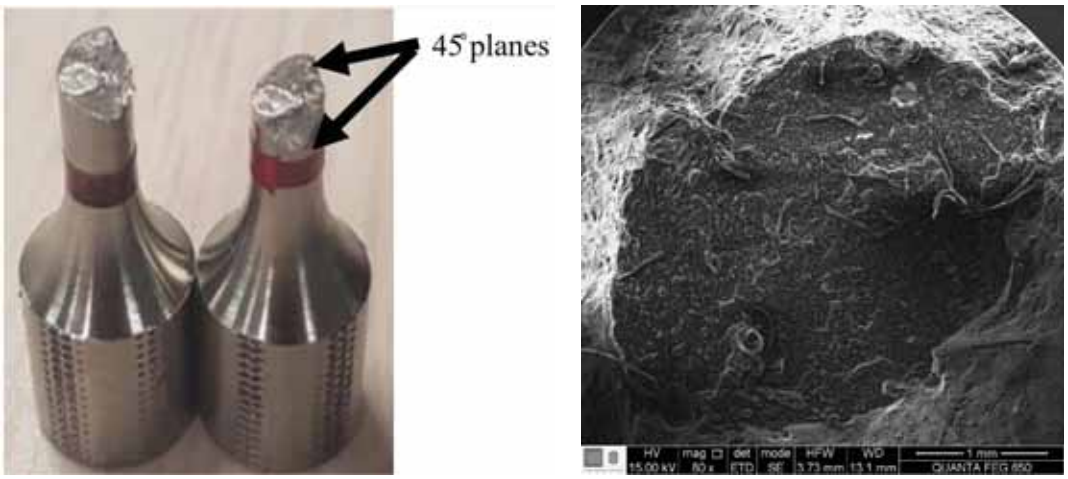

Figure 11. Tensile test: (**a**) macroscopic aspect of the fracture surface; (**b**) shear lips planes.

Figure 12a shows an entirely brittle fracture morphology. In Figure 12b, a fracture surface with a mixed morphology can be seen, known as a "quasi-cleavage", where small diameter dimples [12] are observed. Of note are the brittle areas with cleavage facets, which are divided by large primary cracks. Furthermore, it shows a probable lack of fusion [27] with a width measurement between 2.4 and 5 μm that might be attributed to the EBM process.

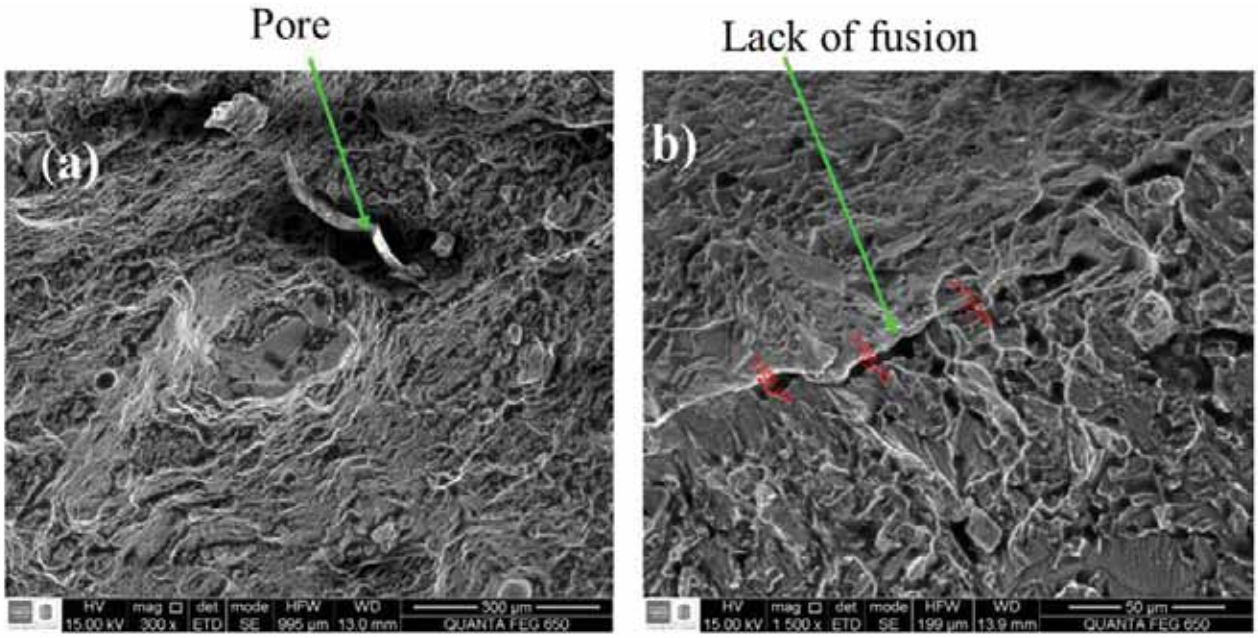

Figure 12. Fracture surface showing: (**a**) porosity defects; (**b**) lack of fusion.

Figure 13a shows the Ti−6Al−4V alloy's fracture surface morphology. The specimen presents several nucleation sites that have been associated with a brittle fracture, and primary and secondary cracks are observed. Different nucleation spots would occur, with at least one probably starting from a lack-of-fusion locus. Additionally, a very deformed structure is observed, indicating an amorphous material, as indicated by [21], thereby conferring brittle behavior. Moreover, Figure 13b shows a mixed fracture surface with a quasi-cleavage formed by small dimples and areas formed by cleavage facets, primary cracks, and large cavities. Likewise, it shows internal lack-of-fusion defects typical for a Ti−6Al−4V EBM specimen. As a result, the fracture zone is observed to have a brittle fracture. In addition, nucleated primary cracks in the surface plane and secondary cracks penetrating the perpendicular plane can be seen, and there is evidence of striations around some primary cracks in the surface, showing apparent plasticity attributed to the dynamism of loading and unloading. Finally, Figure 13c presents a magnified view of the fracture area. It shows the representative fracture surfaces of the specimens that failed from the surface and internal fatigue crack initiation, depicting the corresponding defects.

Figure 14a shows broken sliding planes on a macroscopic scale. Of note are the non-crystalline areas at the right-bottom and left of Figure 14a, whereas the area inside the green square is crystalline as there are what appear to be slipping planes. Once the mechanical load overcomes the weaker zone, the crystalline part cannot withstand the load, so fatigue cracks can propagate by reverse slipping in the maximum shear stress direction. Figure 14b is a close-up of that region. Again, the slip bands appear to be broken. Furthermore, the slender facet feature may be due to the broken sliding planes. According to the literature [10], such a facet could be formed by a cleavage or a slip on the basal plane of the α grain, which is a hexagonal close-packed cell.

Finally, it must be noted that there are spherical microporosities in Figure 12 and in the centers of Figures 13b and 14b, which have been reported for this manufacturing process [3,25], and they have been attributed to atomized inert gas bubbles trapped in the powder [10,27].

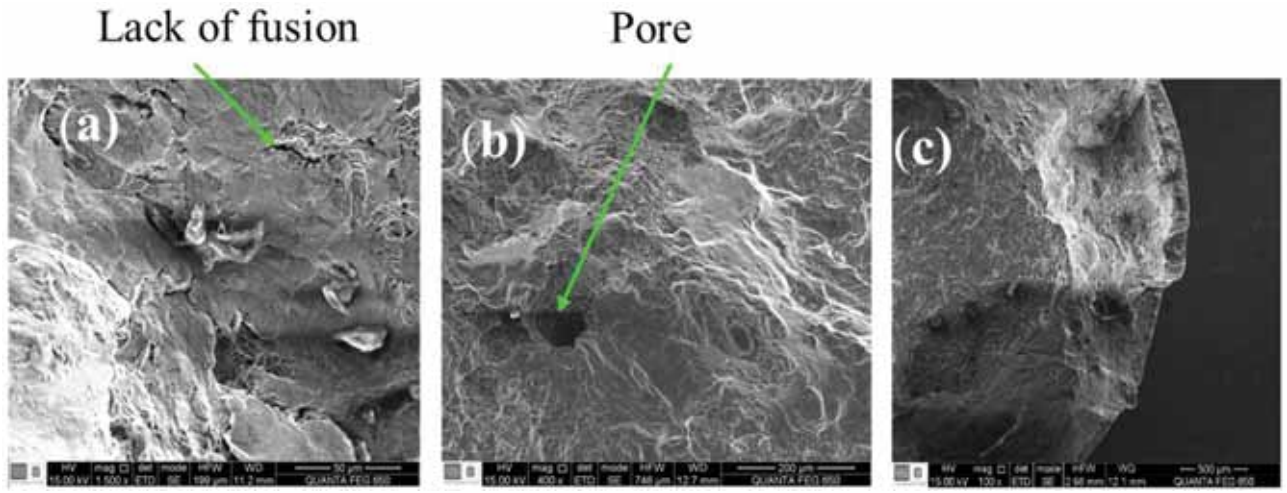

Figure 13. SEM micrographs showing fracture morphology: (**a**) lack of fusion; (**b**) pore on the matrix; (**c**) general view of fractured surface.

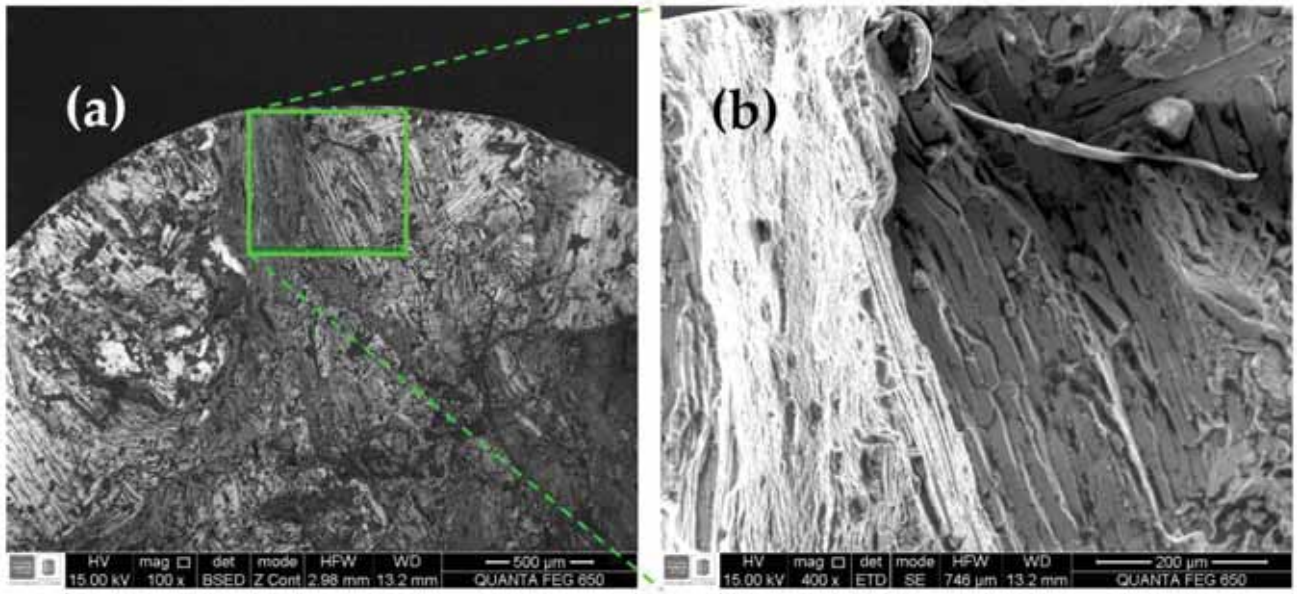

Figure 14. SEM micrographs showing the slipping planes: (**a**) a general view; (**b**) a close-up.

4. Discussion

The behavior observed in Figure 5, where there is a significant plastic elongation but almost no plastic hardening for a metallic material, can be attributed to the manufacturing process used in the specimens. Similar overall results were reported in [17,25,31,37], with [4,26,27,31,37] reporting similar elongation values. As explained in Section 1.1, the manufacturing technique uses an electron beam to selectively melt a metallic powder bed in superimposed layers until the desired topology is achieved. This process may cause the elements used for the alloy to not be evenly distributed. Moreover, because the specimens were machined but not stress-relieved, the reduction in fatigue life is directly attributed to the second cause. This narrows the conclusion of Bourell et al. [21] that as-processed surfaces have a reduced fatigue life.

The Bauschinger effect observed in the stress−strain loops might be explained as follows: Induced cold work causes a buildup of barriers to the movement of dislocations.

When tensions reverse, the dislocations are favored by the stresses present in the dislocation barriers. These barriers are now probably not as strong compared to the previous cycle. Therefore, the dislocations slide easily, resulting in a lower yield strength for plastic deformation in the next load cycle. Moreover, it is visible how the area inside the loops becomes larger as the material is subjected to more loading cycles. This softening was also reported [20,32] for similar AM methods.

The life difference between the AM and the forged materials fades after about 6000 cycles, as seen in Figure 10. This result could be due to a lower incidence of porosity and residual stress as the applied stress is lower, as observed in [28]. Fatemi [39] pointed out that no AM material would match an as-forged material without a surface treatment, and AM alloys can have up to 75% the fatigue performance of wrought parts [15]. Moreover, it is agreed that surface roughness is the culprit of the most significant fatigue life reduction in metal AM [15,19,27]. Such an effect can be minimized by appropriate surface machining and stress relief processes [7]. However, porosity is not always unwelcome, as it could benefit osseointegration.

In the averaged CM, Equation (1), the constants are $b = -2.072$ and $c = -0.536$. Furthermore, the two Ti-specific rules, BS presented in Equation (3) and MC described in Equation (4), are very close in prediction.

The error for the two Ti-specific rules was obtained by comparing each rule to the experimentally obtained strain values. Figure 15 shows the error difference between the BS and MC errors. If the error is negative, the BS error is larger than the MC error, so the MC gives a closer prediction. Conversely, if the error is positive, the MC error is larger than the BS error, so the BS gives a closer prediction. Therefore, the BS rule is slightly closer at shorter lives, whereas MC describes strains that are closer after about 2500 cycles. However, both rules predict strains that are more than 20% smaller than the experimentally observed strains after that number of cycles.

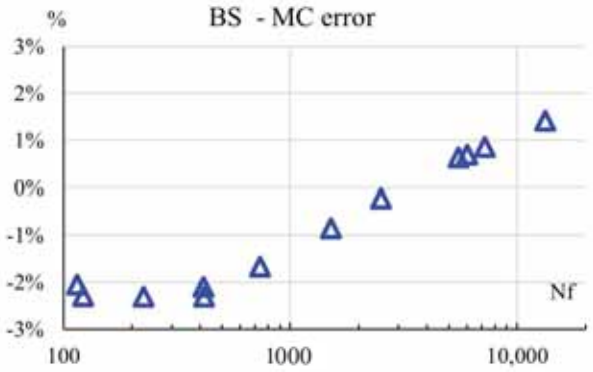

Figure 15. Error difference between the two Ti-specific rules.

The other component that is needed to model the LCF is an appropriate cyclic stress−strain rule. The Ramberg−Osgood model describes a material's dynamic mechanical behavior for the elastic and plastic regions of the stress−strain curve, as shown in Equation (4) as follows:

$$\frac{\Delta\varepsilon}{2} = \frac{\Delta\sigma}{2E} + \left(\frac{\Delta\sigma}{2K'}\right)^{\frac{1}{n'}} \quad (4)$$

The rules of thumb to establish the Ramberg−Osgood constants are described in [9]. If σ_u/σ_y is < 1.2, the material softens cyclically, and n' should be below 0.2. The ratio $EK'/(E+K')$ should be similar to K', which, in this case, is 1038.2. Thus, the data-fitted Ramberg−Osgood constants for Equation (4) are $K' = 1069.15$ and $n' = 0.1965$ for the EBM Ti−6Al−4V alloy. As a comparison, Benz et al. [33] reported 1022 and 0.012, respectively. It should be emphasized that the cyclical Ramberg−Osgood curve only describes the stabilized behavior of the material and does not model the transient softening. Figure 16

depicts the experimental strains ($\Delta\varepsilon_{exp}$) at approximately half of the failure cycle for the specimens and the Ramberg−Osgood model ($\Delta\varepsilon_{RO}$) for the EBM-printed Ti−6Al−4V alloy, assuming the material is of Masing type.

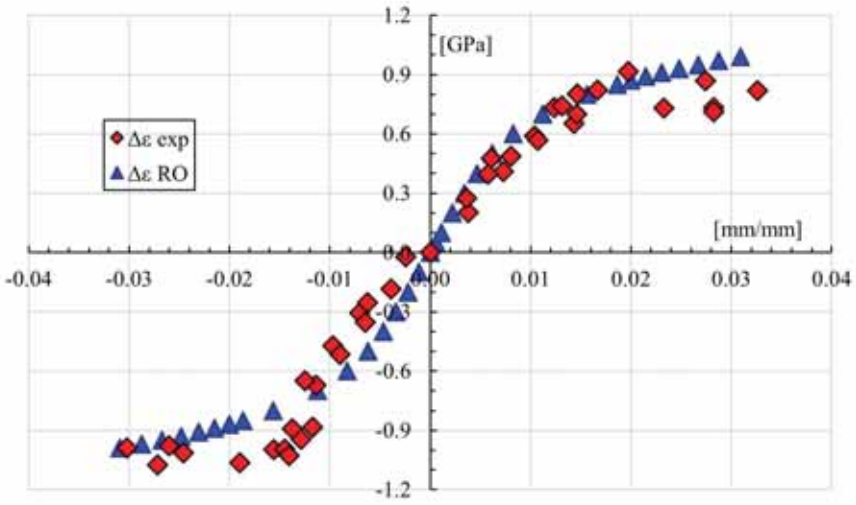

Figure 16. Dynamic stress−strain behavior.

The transient softening behavior of the alloy is shown in Figure 17, where it can be seen how the EBM-printed alloy loses strength at higher lives in both tension and compression. However, for the short lives, significant softening ranges were not observed. Hence, the softening rate depends on $\Delta\varepsilon$ at a reasonably linear rate, as indicated by the dotted lines.

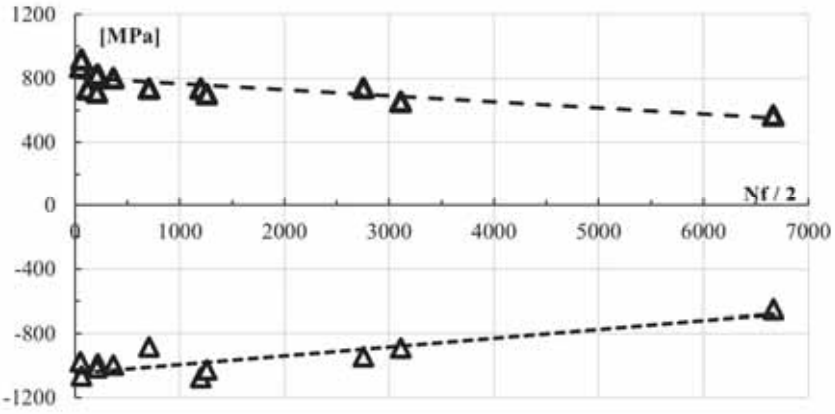

Figure 17. Failure stress at half failure life.

On the other hand, the probable lack of fusion or porosity observed in Figure 12 and the sharpness of the generated defects by the primary and applied alternative stress cracks acted as stress concentrators, which may have caused the pores to open and close repetitively, creating elongated and sharp defects. This combination of events can induce the nucleation of fatigue cracks that ultimately lead to material fracture. In addition, sharp defects are known to act as local stress concentrator factors for a crack to nucleate until it is detectable [40,41].

Slipping planes indicate dislocation movements in a microstructure [40], and persistent slip bands (PSPs) are seen in Figure 14. The PSPs do not represent a microstructural change by their very nature; they are just a consequence of dislocation growth [9,41]. Therefore, these PSPs are the origin of the crack nucleation.

5. Conclusions

From the tensile test results, we found that the yield stress (1023 MPa) and the ultimate stress (1130 MPa) are very close, with an elongation in the plastic regime of 8.2%, which indicates that the material does not exhibit work hardening. Moreover, from the hysteresis loops, a typical behavior for brittle metals was observed, which tend to soften when subjected to fully inverted loads. The cyclically imposed strain causes a rearrangement of the dislocations, which makes the material weaker to sustain deformation, thereby softening the material. The EBM melts the metallic powder, forming the sought topology layer by layer, which does not allow the particles to coalesce, possibly giving the material a fragile behavior. However, the Ti−6Al−4V alloy presented about 8.2% of plastic elongation for a total elongation of 9% in the tensile test. This phenomenon can be attributed to the manufacturing process. Since the specimens were EBM-manufactured, the high thermal gradients caused the formation of different crack sizes, which generated this particular behavior. Finally, when significant plastic deformation is introduced at any point, the Bauschinger effect must be considered.

The acquired low-cycle data was processed and adjusted to a type of Coffin−Manson rule with averaged constants $b = -2.072$ and $c = -0.536$. When performing the logarithmic data regression for the obtained Coffin−Manson rule, the elastic deformation curve shows a growing trend, which is attributed to the material presenting micro-fractures as it was subjected to a controlled cyclic strain and also to the manufacturing process. The EBM process melts metal powders, which causes the material to have a greater porosity when compared to other types of conventional manufacturing, such as forging. Furthermore, inversely proportional behavior was observed in the low-cycle regime. As the number of cycles increased, the strain decreased. Moreover, it was confirmed that the Baumel−Seager and Meggiolaro−Castro rules are suitable for a closer description of the low-cycle regime for the studied alloys. Finally, the obtained Ramberg−Osgood constants were $K' = 1069.15$ and $n' = 0.1965$; these can be used to model strain loops and the crack initiation process.

Under high strain conditions, a material failure analysis concluded that the Ti−6Al−4V alloy exhibited possible fragile behavior in such a way that it was possible to identify the areas of failure in the fractured areas of the specimens. In the microfractographic analysis, it was observed that the morphology of the failed specimens due to fatigue showed secondary cracks from the nucleation. This condition is due to the high deformation that the material has sustained. Moreover, it was seen that the specimen presented one lobe that formed an amorphous structure, which gives a fragile behavior to the specimen.

Author Contributions: Conceptualization, A.D.P.-C. and E.M.-D.; methodology, A.D.P.-C. and J.G.D.-R.; software, J.G.D.-R.; validation, J.G.D.-R.; formal analysis J.G.D.-R., A.D.P.-C. and E.M.-D.; investigation, O.A.G.-E.; resources, D.F.V.-B. and E.M.-D.; data curation, D.F.V.-B. and J.G.D.-R.; writing—original draft preparation, J.G.D.-R.; writing—review and editing, A.D.P.-C., J.G.D.-R. and O.A.G.-E.; visualization, O.A.G.-E.; supervision, A.D.P.-C.; project administration, A.D.P.-C.; funding acquisition, All. All authors have read and agreed to the published version of the manuscript.

Funding: This research was funded by Universidad Industrial de Santander, grants VIE 2827 and VIE 3716.

Data Availability Statement: The data presented in this study are available on request from the corresponding author.

Acknowledgments: The support of L. Gutierrez and F.A. Jiménez in performing some of the tests and the Center for Electron Microscopy at UIS is greatly appreciated.

Conflicts of Interest: The authors declare no conflict of interest.

Nomenclature

AM	additive manufacturing
EBM	electron beam melting
ε_e	elastic strain
ε_p	plastic strain
σ'_f	true stress
σ_u	ultimate stress
σ_y	yield stress
σ_f	fracture stress
Nf	number of cycles to failure
b, c	material dependent constants for the Coffin−Manson rule
R	load inversion rate
X, Y	directions perpendicular to printing
Z	printing direction

References

1. Wanjara, P.; Backman, D.; Sikan, F.; Gholipour, J.; Amos, R.; Patnaik, P.; Brochu, M. Microstructure and Mechanical Properties of Ti-6Al-4V Additively Manufactured by Electron Beam Melting with 3D Part Nesting and Powder Reuse Influences. *J. Manuf. Mater. Process.* **2022**, *6*, 21. [CrossRef]
2. Yates, J.R.; Efthymiadis, P.; Antonysamy, A.A.; Pinna, C.; Tong, J. Do additive manufactured parts deserve better? *Fatigue Fract. Eng. Mater. Struct.* **2019**, *42*, 2146–2154. [CrossRef]
3. Rafi, H.K.; Karthik, N.V.; Gong, H.; Starr, T.L.; Stucker, B.E. Microstructures and Mechanical Properties of Ti6Al4V Parts Fabricated by SLM and EBM. *J. Mater. Eng. Perform.* **2013**, *22*, 3872–3883. [CrossRef]
4. Frazier, W.E. Metal Additive Manufacturing: A Review. *J. Mater. Eng. Perform.* **2014**, *23*, 1917–1928. [CrossRef]
5. Obermayer, T.; Krempaszky, C.; Werner, E. Analysis of Texture and Anisotropic Elastic Properties of Additively Manufactured Ni-Base Alloys. *Metals* **2022**, *12*, 1991. [CrossRef]
6. Erdakov, I.; Glebov, L.; Pashkeev, K.; Bykov, V.; Bryk, A.; Lezin, V.; Radionova, L. Effect of the Ti6Al4V Alloy Track Trajectories on Mechanical Properties in Direct Metal Deposition. *Machines* **2020**, *8*, 79. [CrossRef]
7. Beretta, S.; Romano, S. A comparison of fatigue strength sensitivity to defects for materials manufactured by AM or traditional processes. *Int. J. Fatigue.* **2017**, *94*, 178–191. [CrossRef]
8. Tamayo, J.A.; Riascos, M.; Vargas, C.A.; Baena, L.M. Additive manufacturing of Ti6Al4V alloy via electron beam melting for the development of implants for the biomedical industry. *Heliyon* **2021**, *7*, e06892. [CrossRef]
9. Castro, J.T.P.; Meggiolaro, M.A. *Fatigue Design Techniques*, 3rd ed.; CreateSpace: Scotts Valley, CA, USA, 2016.
10. Liu, S.; Shin, Y.C. Additive manufacturing of Ti_6Al_4V alloy: A review. *Mater. Des.* **2019**, *164*, 107552. [CrossRef]
11. Corredor, E.; González-Estrada, O.A.; Ospina-Ospina, R. Deposición de láser pulsado de hidroxiapatita en Ti-6Al-4V producido por manufactura aditiva. *Rev. UIS Ing.* **2022**, *21*, 107–122.
12. González-Estrada, O.A.; Pertuz Comas, A.D.; Ospina, R. Characterization of hydroxyapatite coatings produced by pulsed-laser deposition on additive manufacturing Ti6Al4V ELI. *Thin Solid Films* **2022**, *763*, 139592. [CrossRef]
13. León, B.J.; Díaz-Rodríguez, J.G.; González-Estrada, O.A. Daño en partes de manufactura aditiva reforzadas por fibras continuas. *Rev. UIS Ing.* **2020**, *19*, 161–175. [CrossRef]
14. Parrado-Agudelo, J.Z.; Narváez-Tovar, C. Mechanical characterization of polylactic acid, polycaprolactone and Lay-Fomm 40 parts manufactured by fused deposition modeling, as a function of the printing parameters. *ITECKNE* **2019**, *16*, 25–31. [CrossRef]
15. Fatemi, A.; Molaei, R.; Sharifimehr, S.; Shamsaei, N.; Phan, N. Torsional fatigue behavior of wrought and additive manufactured Ti-6Al-4V by powder bed fusion including surface finish effect. *Int. J. Fatigue* **2017**, *99*, 187–201. [CrossRef]
16. Wang, P.; Sin, W.J.; Nai, M.L.S.; Wei, J. Effects of Processing Parameters on Surface Roughness of Additive Manufactured Ti-6Al-4V via Electron Beam Melting. *Materials* **2017**, *10*, 1121. [CrossRef]
17. Günther, J.; Krewerth, D.; Lippmann, T.; Leuders, S.; Tröster, T.; Weidner, A.; Biermann, H.; Niendorf, T. Fatigue life of additively manufactured Ti–6Al–4V in the very high cycle fatigue regime. *Int. J. Fatigue* **2017**, *94*, 236–245. [CrossRef]
18. Meggiolaro, M.; de Castro, J.T.P. Statistical evaluation of strain-life fatigue crack initiation predictions. *Int. J. Fatigue* **2004**, *26*, 463–476. [CrossRef]
19. Chastand, V.; Quaegebeur, P.; Maia, W.; Charkaluk, E. Comparative study of fatigue properties of Ti-6Al-4V specimens built by electron beam melting (EBM) and selective laser melting (SLM). *Mater. Charact.* **2018**, *143*, 76–81. [CrossRef]
20. Agius, D.; Kourousis, K.I.; Wallbrink, C. Elastoplastic response of as-built SLM and wrought Ti-6Al-4V under symmetric and asymmetric strain-controlled cyclic loading. *Rapid. Prototyp. J.* **2018**, *24*, 1409–1420. [CrossRef]
21. Bourell, D.; Kruth, J.P.; Leu, M.; Levy, G.; Rosen, D.; Beese, A.M.; Clare, A. Materials for additive manufacturing. *CIRP Ann.* **2017**, *66*, 659–681. [CrossRef]
22. Kasperovich, G.; Hausmann, J. Improvement of fatigue resistance and ductility of TiAl6V4 processed by selective laser melting. *J. Mater. Process. Technol.* **2015**, *220*, 202–214. [CrossRef]

23. Le, V.-D.; Pessard, E.; Morel, F.; Prigent, S. Fatigue behaviour of additively manufactured Ti-6Al-4V alloy: The role of defects on scatter and statistical size effect. *Int. J. Fatigue* **2020**, *140*, 105811. [CrossRef]
24. Biswas, N.; Ding, J.L.; Balla, V.K.; Field, D.P.; Bandyopadhyay, A. Deformation and fracture behavior of laser processed dense and porous Ti6Al4V alloy under static and dynamic loading. *Mater. Sci. Eng. A* **2012**, *549*, 213–221. [CrossRef]
25. de Formanoir, C.; Michotte, S.; Rigo, O.; Germain, L.; Godet, S. Electron beam melted Ti–6Al–4V: Microstructure, texture and mechanical behavior of the as-built and heat-treated material. *Mater. Sci. Eng. A* **2016**, *652*, 105–119. [CrossRef]
26. Hrabe, N.; Gnäupel-Herold, T.; Quinn, T. Fatigue properties of a titanium alloy (Ti–6Al–4V) fabricated via electron beam melting (EBM): Effects of internal defects and residual stress. *Int. J. Fatigue* **2017**, *94*, 202–210. [CrossRef]
27. Kahlin, M.; Ansell, H.; Moverare, J.J. Fatigue behaviour of notched additive manufactured Ti6Al4V with as-built surfaces. *Int. J. Fatigue* **2017**, *101*, 51–60. [CrossRef]
28. Franchitti, S.; Pirozzi, C.; Borrelli, R. Influence of hot isostatic pressing and surface finish on the mechanical behaviour of Ti6Al4V processed by electron beam melting. *Fatigue Fract. Eng. Mater. Struct.* **2020**, *43*, 2828–2841. [CrossRef]
29. Toasa Caiza, P.D.; Sire, S.; Ummenhofer, T.; Uematsu, Y. Low cost estimation of Wöhler and Goodman–Haigh curves of Ti-6Al-4V samples by considering the stress ratio effect. *Fatigue Fract. Eng. Mater. Struct.* **2021**, *45*, 441–450. [CrossRef]
30. Chern, A.H.; Nandwana, P.; Yuan, T.; Kirka, M.M.; Dehoff, R.R.; Liaw, P.K.; Duty, C.E. A review on the fatigue behavior of Ti-6Al-4V fabricated by electron beam melting additive manufacturing. *Int. J. Fatigue* **2019**, *119*, 173–184. [CrossRef]
31. Sterling, A.; Shamsaei, N.; Torries, B.; Thompson, S.M. Fatigue Behaviour of Additively Manufactured Ti-6Al-4 v. *Procedia Eng.* **2015**, *133*, 576–589. [CrossRef]
32. Bressan, S.; Ogawa, F.; Itoh, T.; Berto, F. Low cycle fatigue behavior of additively manufactured Ti-6Al-4V under non-proportional and proportional loading. *Frattura Ed. Integrità Strutturale* **2019**, *13*, 18–25. [CrossRef]
33. Radlof, W.; Benz, C.; Heyer, H.; Sander, M. Monotonic and Fatigue Behavior of EBM Manufactured Ti-6Al-4V Solid Samples: Experimental, Analytical and Numerical Investigations. *Materials* **2020**, *13*, 4642. [CrossRef] [PubMed]
34. Bai, C.; Lan, L.; Xin, R.; Gao, S.; He, B. Microstructure evolution and cyclic deformation behavior of Ti-6Al-4 V alloy via electron beam melting during low cycle fatigue. *Int. J. Fatigue* **2022**, *159*, 106784. [CrossRef]
35. Zhang, P.; Z.Zhang, D.; Zhong, B. Constitutive and damage modelling of selective laser melted Ti-6Al-4V lattice structure subjected to low cycle fatigue. *Int. J. Fatigue* **2022**, *159*, 106800. [CrossRef]
36. Carrion, P.E.; Shamsaei, N. Strain-based fatigue data for Ti–6Al–4V ELI under fully-reversed and mean strain loads. *Data Brief.* **2016**, *7*, 12–15. [CrossRef]
37. Galarraga, H.; Warren, R.J.; Lados, D.A.; Dehoff, R.R.; Kirka, M.M.; Nandwana, P. Effects of heat treatments on microstructure and properties of Ti-6Al-4V ELI alloy fabricated by electron beam melting (EBM). *Mater. Sci. Eng. A* **2017**, *685*, 417–428. [CrossRef]
38. Greitemeier, D.; Palm, F.; Syassen, F.; Melz, T. Fatigue performance of additive manufactured TiAl6V4 using electron and laser beam melting. *Int. J. Fatigue* **2017**, *94*, 211–217. [CrossRef]
39. Molaei, R.; Fatemi, A.; Sanaei, N.; Pegues, J.; Shamsaei, N.; Shao, S.; Li, P.; Warner, D.; Phan, N. Fatigue of additive manufactured Ti-6Al-4V, Part II: The relationship between microstructure, material cyclic properties, and component performance. *Int. J. Fatigue* **2020**, *132*, 105363. [CrossRef]
40. Téllez Fontecha, G.E.; Díaz, R.J.G. Análisis de falla del árbol de levas de un motor de seis cilindros en línea. *ITECKNE* **2009**, *6*, 56–62. [CrossRef]
41. Pantazopoulos, G. A Short Review on Fracture Mechanisms of Mechanical Components Operated under Industrial Process Conditions: Fractographic Analysis and Selected Prevention Strategies. *Metals* **2019**, *9*, 148. [CrossRef]